Sub-4 nm PtZn Intermetallic Nanoparticles for Enhanced Mass and Specific Activities in Catalytic Electro-Oxidation Reaction

Zhiyuan Qi,[†] Chaoxian Xiao,[†] Cong Liu,[#] Tian-Wei Goh,[†] Lin Zhou,[‡] Raghu Maligal-Ganesh,[†] Yuchen Pei,[†] Xinle Li,[†] Larry A. Curtiss,[§] Wenyu Huang[*, †, ‡]

[†] Department of Chemistry, Iowa State University, Ames, Iowa, 50011, United States

[‡] Ames Laboratory, U.S. Department of Energy, Ames, Iowa, 50011, United States

[#] Chemical Sciences and Engineering Division, Argonne National Laboratory, Lemont, Illinois, 60439, United States

[§] Materials Science Division, Argonne National Laboratory, Lemont, Illinois, 60439, United States

ABSTRACT: Atomically ordered intermetallic nanoparticles (iNPs) have sparked considerable interest in fuel cell applications by virtue of their exceptional electronic and structural properties. However, the synthesis of small iNPs in a controllable manner remains a formidable challenge because of the high temperature generally required in the formation of intermetallic phases. Here we report a general method for the synthesis of PtZn iNPs (3.2 ± 0.4 nm) on multi-walled carbon nanotubes (MWNT) via a facile and capping agent-free strategy using a sacrificial mesoporous silica ($mSiO_2$) shell. The as-prepared PtZn iNPs exhibited ca. 10 times higher mass activity in both acidic and basic solution towards the methanol oxidation reaction (MOR) compared to larger PtZn iNPs synthesized on MWNT without the $mSiO_2$ shell. Density functional theory (DFT) calculations predict that PtZn systems go through a "non-CO" pathway for MOR because of the stabilization of the OH* intermediate by Zn atoms, while a pure Pt system forms highly stable COH* and CO* intermediates, leading to catalyst deactivation. Experimental studies on the origin of the backward oxidation peak of MOR coincide well with DFT predictions. Moreover, the calculations demonstrate that MOR on smaller PtZn iNPs is energetically more favorable than larger iNPs, due to their high density of corner sites and lower-lying energetic pathway. Therefore, smaller PtZn iNPs not only increase the number but also enhance the activity of the active sites in MOR than larger ones. This work opens a new avenue for the synthesis of small iNPs with more undercoordinated and enhanced active sites for fuel cell applications.

INTRODUCTION

Intermetallic nanomaterials, featuring atomically ordered crystal structures and unique electronic/structural properties, have been garnering increasing research attention in past decades. Tremendous endeavors have been devoted to the investigation of intermetallic nanomaterials, particularly Pt-based, as fuel cell electrocatalysts with the aim of decreasing Pt usage, increasing poisoning tolerance and improving the catalysts activities and stabilities. A great many scientific efforts have been devoted to the preparation of Pt-based alloys and intermetallic compounds, such as PtSn,[1] PtTi,[2-3] PtMn,[4-5] PtCo,[6-8] PtFe,[9-10] PtBi,[11-12] PtPb,[11,13] Pt_3Ni,[5,14] PtZn,[15-18] and PtCu,[19-22] in the electro-oxidation of methanol or formic acid and electroreduction of oxygen.

Among aforementioned intermetallic compounds, PtZn iNPs have been proven as active catalysts toward formic acid and methanol electrooxidation.[15] Regarding the synthesis of intermetallic PtZn, DiSalvo et al. reported the synthesis of PtZn iNPs by reaction of Pt nanoparticles with Zn vapor, and Murray et al. demonstrated the formation of Pt_3Zn intermetallic NCs. However, since the formation of the intermetallic phase usually requires the use of a high-temperature annealing (e.g., 600 °C for Pt_3Zn),[16] the aggregation of nanoparticles, either unprotected or capped with organic capping agents, is unavoidable. The aggregation also adversely renders PtZn iNPs with a broad size distribution ranging from 3 to 15 nm.[15-17] The larger particles limit catalytic activity due to their low surface to volume ratio, and thus hamper the effective utilization of precious metals. The lack of size control can also complicate the product selectivity in size-sensitive reactions. Therefore, the development of a new synthetic strategy to obtain well-defined and small PtZn iNPs is highly desired. To the best of our knowledge, there is no general method available for the synthesis of small iNPs.

Herein, we report the synthesis of small and uniform PtZn iNPs (3.2 ± 0.4 nm) supported on a conductive support (MWNTs), and their electro-oxidation activity is largely enhanced beneficial from such small size and dramatic monodispersity. These PtZn iNPs are capping agent-free and thus have a strong metal-support interaction with MWNTs. We used the mesoporous silica ($mSiO_2$) shell to

prevent iNPs from aggregation during the high-temperature annealing to form the PtZn intermetallic phase (denoted as PtZn/MWNT@$mSiO_2$). This strategy has not been applied to synthesis iNPs supported on conductive supports.[23-29] On the contrast, the unprotected PtZn nanoparticles supported on MNWTs (denoted as PtZn/MWNT) experienced severe aggregation during annealing, and the formed PtZn iNPs have an average diameter of 27 nm. DFT calculations and experimental results have proved that the smaller iNPs are energetically more favorable for methanol oxidation reaction (MOR) and thus have enhanced both specific and mass activities in comparison to larger iNPs synthesized by a traditional wetness impregnation method without the $mSiO_2$ capping shell.

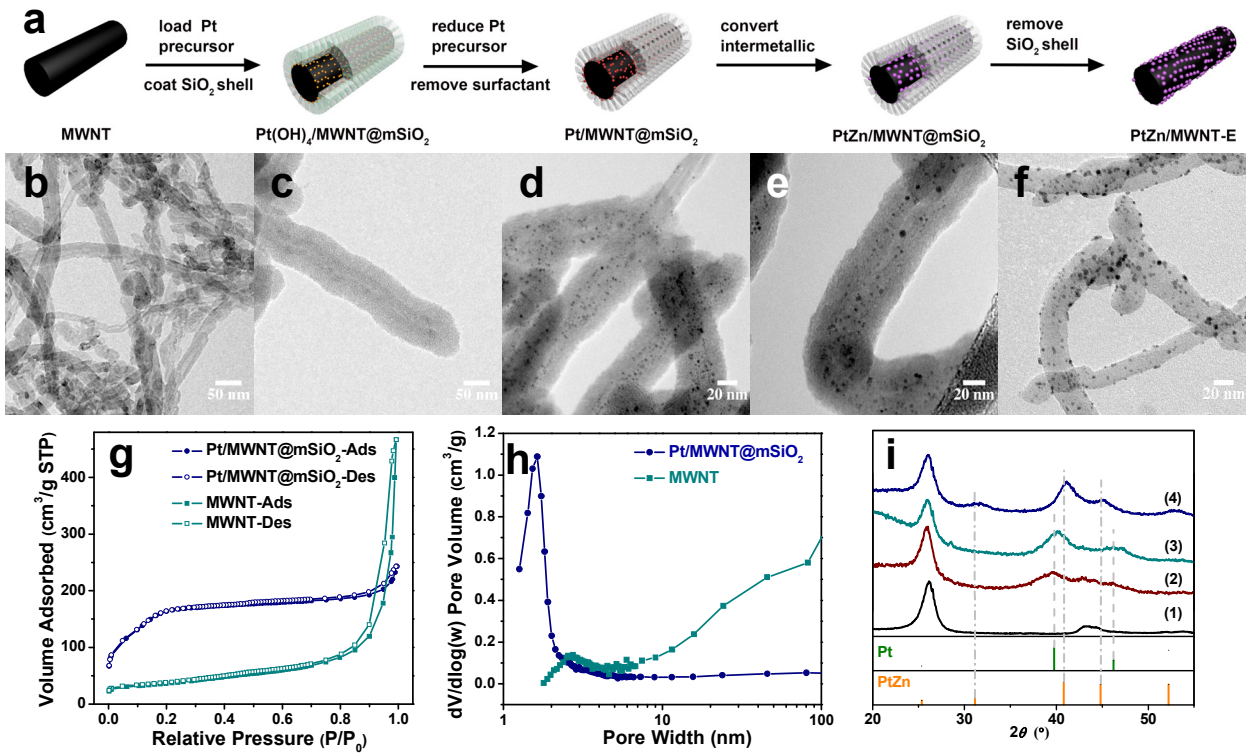

Figure 1. (a) Schematic representation of the synthesis route to PtZn/MWNT@$mSiO_2$. (b-f) TEM images of (b) pristine MWNT, (c) $Pt(OH)_4$/MWNT@SiO_2 formed after loading Pt and coating silica, (d) Pt/MWNT@$mSiO_2$ after H_2 reduction, (e) PtZn/MWNT@$mSiO_2$ prepared by annealing at 600 °C, and (f) PtZn/MWNT-E after etching away the $mSiO_2$ shell. (g) Nitrogen adsorption and desorption isotherm of MWNT and Pt/MWNT@$mSiO_2$. (h) BJH pore size distribution of MWNT and Pt/MWNT@$mSiO_2$. (i) PXRD patterns of (i-1) pristine MWNT, (i-2) Pt/MWNT@$mSiO_2$ reduced at 240 °C, (i-3) PtZn/MWNT@$mSiO_2$ prepared by solvothermal synthesis at 330 °C, and (i-4) PtZn/MWNT@$mSiO_2$ annealed at 600 °C.

RESULTS AND DISCUSSION

The preparation of MWNT supported PtZn iNPs was summarized in Figure 1a. $Pt(OH)_4$/MWNT@$mSiO_2$ was prepared using the precipitation-deposition method followed by $mSiO_2$ coating and H_2 reduction to form Pt/MWNT@$mSiO_2$. A Zn precursor was introduced into the Pt/MWNT@$mSiO_2$ to form $mSiO_2$-encapsulated PtZn alloy nanoparticles.[28] After separating the alloy nanoparticles from the solution, we annealed them at 600 °C to form the ordered iNP PtZn/MWNT@$mSiO_2$. Finally, the insulating $mSiO_2$ shell was etched to test the PtZn/MWNT for electrocatalytic MOR.

To deposit Pt onto MWNT, chloroplatinic acid (H_2PtCl_6), MWNT and urea aqueous mixture were heated to 90 °C, at which temperature urea slowly decomposed to generate hydroxide ions (OH^-). The OH^- ions homogeneously precipitated Pt(IV) onto MWNT (denoted as $Pt(OH)_4$/MWNT).[30] The pH of the solution changed from 3 to 8, indicating the successful decomposition of urea and precipitation of Pt ions. The $mSiO_2$ shell was then coated on the $Pt(OH)_4$/MWNT by a sol-gel method using cetyltrimethylammonium bromide (CTAB) as the pore-directing agent. Figure 1b shows transmission electron microscopy (TEM) images of the pristine MWNT with an outer diameter in the range of 30-50 nm. After loading $Pt(OH)_4$, a 15 nm thick $mSiO_2$ shell was uniformly coated on MWNTs (Figure 1c). The deposited $Pt(OH)_4$ species was further reduced by 50 mL/min of 10% H_2 in an argon flow at 240 °C to form Pt nanoparticles. After removing CTAB surfactants by methanol refluxing to open the channels in the $mSiO_2$

shell, Pt/MWNT@$mSiO_2$ was obtained (Figure 1d). With the $mSiO_2$ shell inhibiting the aggregation, as-form Pt nanoparticles have an average diameter of 2.1 ± 0.3 nm (Figure S2a). These Pt nanoparticles were also evenly dispersed at the interface between the MWNT and $mSiO_2$ shell (Figure 1d), which indicates a strong interaction between Pt and MWNT. To prove this strong interaction, a control sample was prepared by loading polyvinylpyrrolidone (PVP)-capped Pt nanoparticles onto MWNT, followed by silica coating. As shown in Figure S3b, many Pt particles were not well confined at the interface between MWNT and $mSiO_2$, which could be easily detached from MWNT during silica etching.

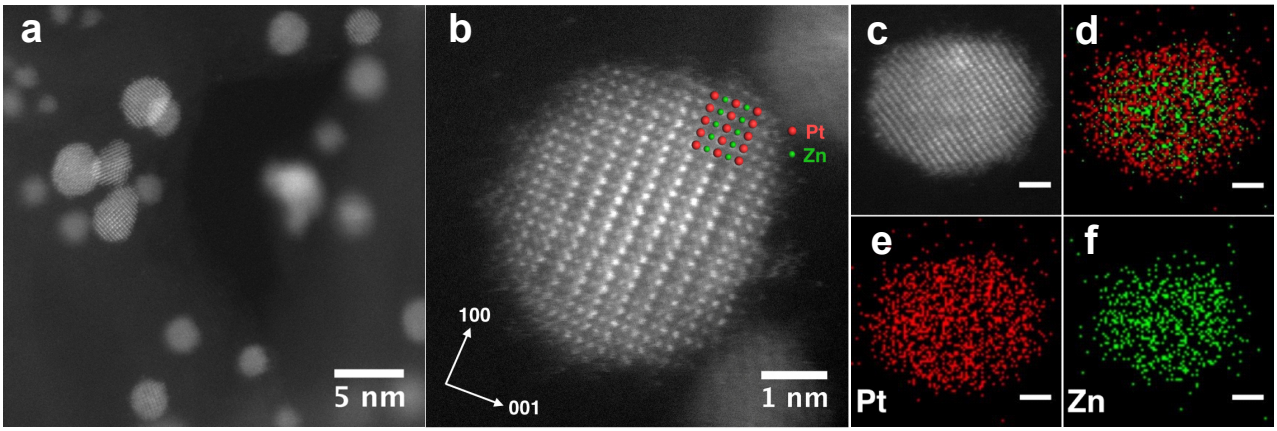

Figure 2. (a, b) High-resolution HAADF STEM images of PtZn iNPs. The red and green spheres in Figure 2b represent Pt and Zn atoms. (c) HAADF-STEM image of a single PtZn iNP. (d-f) Elemental mappings of Pt versus Zn (d), Pt (e), Zn (f). Scale bar, 1 nm.

N_2 sorption was measured to verify the mesoporous structure of the $mSiO_2$ shell (Figure 1g). Pristine MWNT shows weak adsorption of N_2 at lower relative pressure (P/P_0) until P/P_0 = 0.8 where an upward adsorption occurs, which leads to a small Brunauer-Emmett-Teller (BET) surface area of 129 m^2/g. After coating the $mSiO_2$ shell on the MWNT, the BET surface area of Pt/MWNT@$mSiO_2$ increases to 633 m^2/g. Pt/MWNT@$mSiO_2$ exhibits a type-IV isotherm with a small capillary condensation step, indicating the existence of a mesoporous structure of the $mSiO_2$ shell. Based on the Barrett-Joyner-Halenda (BJH) pore size distribution (Figure 1h) the average pore diameter of the $mSiO_2$ is 1.8 nm, with a small amount of mesopores. The average pore diameter of the $mSiO_2$ shell matches the size of formed Pt nanoparticles, which suggests that the mesopore in the $mSiO_2$ shell restricts the growth of the confined Pt nanoparticles under reduction.

To introduce Zn, the Pt/MWNT@$mSiO_2$ was redispersed with $Zn(acac)_2$ (Pt:Zn molar ratio = 1:1) in oleic acid and oleylamine mixture, heated to 330 °C and maintained at this temperature for 1 h. The reaction was monitored by powder X-ray diffraction (PXRD) as shown in Figure 1i. At 330 °C, we observed the formation of PtZn alloy nanoparticles. Only after annealing at 600 °C, we observed the formation of ordered intermetallic PtZn phase. Due to the small size of nanoparticles, only peaks before 2θ = 60° can be clearly observed. As shown in Figure 1i-3, Pt/MWNT@$mSiO_2$ has broad peaks at 39.8° and 46.2°, indicating the formation of small Pt nanoparticles after the reduction of $Pt(OH)_4$/MWNT@$mSiO_2$. The intense diffraction peak around 26° is assigned to graphitic carbon (002) from MWNT, as confirmed by PXRD pattern of pristine MWNT. Before annealing at 600 °C, the fresh alloy PtZn/MWNT@$mSiO_2$ (Figure 1i-3) shows that the Pt diffraction peak at 39.8° slightly shifts towards higher diffraction angle. This shift is due to the decreased lattice constant after incorporation of Zn into Pt to form PtZn alloy. After annealing at 600 °C, a completely different set of diffraction peaks are formed (31.1°, 40.8°, 44.8°, and 53.4°) as shown by pattern (4) in Figure 1i. This set of diffraction peaks corresponds well with the standard PXRD pattern of intermetallic PtZn ($P4/mmm$), which has the tetragonal AuCu ($L1_0$ type) structure. However, all diffraction peaks have a slight shift to higher angle compared with the standard pattern of intermetallic PtZn. We are currently investigating the origin of this shift and we believe this shift can be attributed to the ultrasmall size of the formed PtZn iNPs. The actual Pt:Zn molar ratio measured by inductively coupled plasma mass spectrometry (ICP-MS) is 1.03 ± 0.01, which indicate all added Zn from the precursor is incorporated into the final PtZn iNPs.

Using the Debye–Scherrer equation, the average size for PtZn iNPs in PtZn/MWNT@$mSiO_2$ was calculated as 3.2 nm, which is in good agreement with TEM measurements (Figure 1e-f and Figure S2b). To prove that $mSiO_2$ shell can effectively constrain the size and prevent the aggregation of metal nanoparticles, MWNT-supported Pt nanoparticles were prepared using the same precipitation method in the absence of $mSiO_2$ shell. After the same reduction treatment, Pt nanoparticles with average size of 3.7 ± 0.9 nm was observed from TEM images (Figure S4c and Table S1), which is almost double in size compared to Pt nanoparticles in Pt/MWNT@$mSiO_2$. Particle sizes of 27 ± 20 nm were

observed for PtZn/MWNT (Figure S4d), prepared by wetness impregnation method without the $mSiO_2$ shell, which is nearly thirteen times larger than those prepared with the confinement of $mSiO_2$. Moreover, the particle size distribution also increased significantly without the confinement of the $mSiO_2$ shell. Even though PXRD (Figure S5) also shows the formation of PtZn phases in the absence of $mSiO_2$, it is clearly seen that both Pt and PtZn nanoparticles have larger sizes and broader size distributions compared to those prepared with the protection of the $mSiO_2$ shell. We thus suggest that the $mSiO_2$ shell can successfully restrict the growth of PtZn nanoparticles and significantly prevent them from aggregation under high-temperature annealing, required for the transition from the PtZn alloy to the intermetallic phase. Besides, the strong capping agents (i.e. oleylamine and oleic acid) could be removed during the 600 °C annealing. A detailed FTIR study (Figure S6) was conducted to confirm the organic capping agent-free nature of PtZn iNPs. This approach could be used to prepare electrocatalysts of different compositions with clean surfaces.

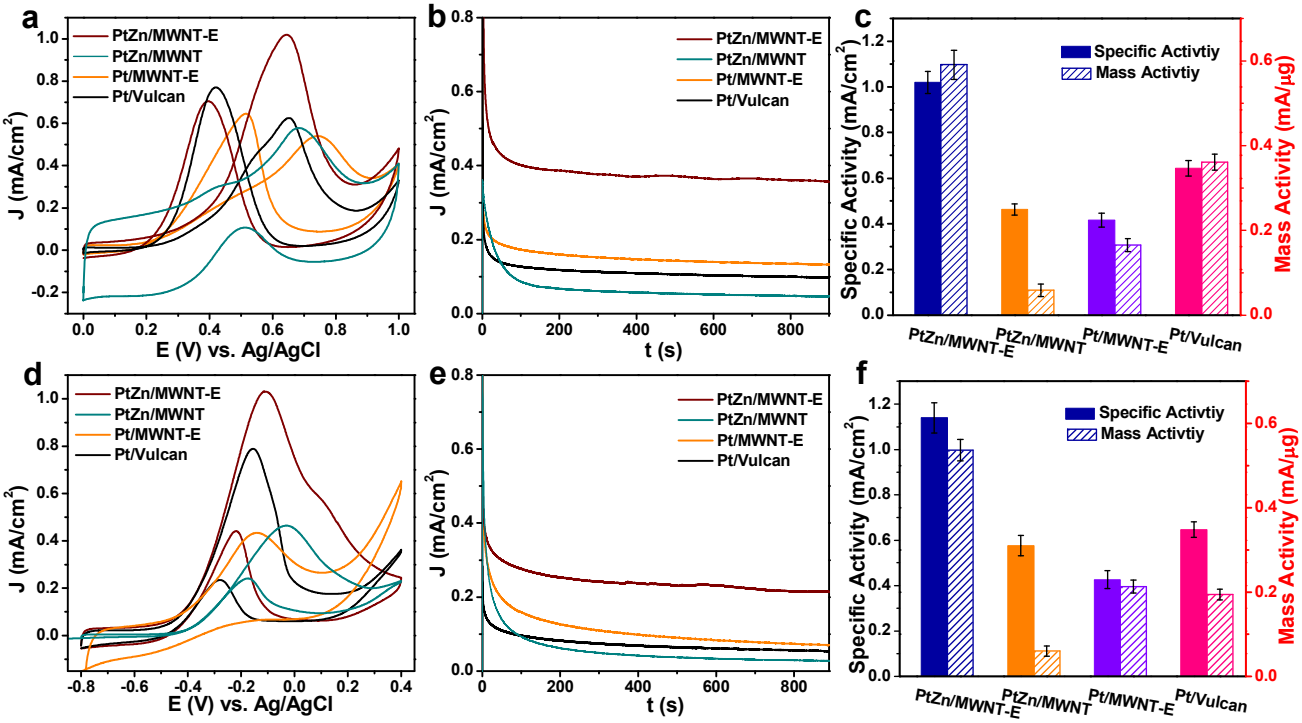

Figure 3. Cyclic voltammetry (a) and chronoamperometry (b) of PtZn/MWNT-E, Pt/MWNT-E, PtZn/MWNT (synthesized in the absence of $mSiO_2$) and commercial Pt/Vulcan catalysts measured at room temperature in argon-purged 0.5 M H_2SO_4 and 1 M methanol. (c) Specific activity and mass activity at 0.65 V vs. Ag/AgCl reference electrode, Cyclic voltammetry (d) and chronoamperometry (e) of PtZn/MWNT-E, Pt/MWNT-E, PtZn/MWNT (synthesized in absence of $mSiO_2$) and commercial Pt/Vulcan catalysts measured at room temperature in argon-purged 0.1 M KOH and 0.5 M methanol. (f) Specific activity and mass activity at -0.1 V vs. Ag/AgCl electrode, all the measurements were repeated 3 times and currents were normalized to the electrochemical surface area (ECSA).

The homogenous PtZn intermetallic structure is further confirmed by high-angle-annular-dark-field (HAADF) scanning transmission electron microscopy (STEM) imaging and energy-dispersive X-ray spectroscopy (EDS) elemental mapping using an aberration-corrected electron microscope. In Figure 2a, all PtZn iNPs in focus showed clear lattice fringes, indicating good crystallinity. A PtZn iNP is viewed along [010] zone axis in Figure 2b. The ordered intermetallic structure at the center of the NP is showed by alternating bright (Pt column) and darker (Zn column) contrast on {001} planes, due to greater electron scattering to large detector collection angles by heavier atoms. The two atomic plane distances were measured as 0.354 nm and 0.203 nm, which is in good agreement with the lattice spacing of intermetallic PtZn ($P4/mmm$) along [001] and [200] directions. EDS elemental mapping of as-formed PtZn iNPs was also obtained (Figure 2 c-f), which shows that the Pt map (Figure 2e) has a slightly larger area than the Zn map (Figure 2f), indicating a Pt-rich layer on the surface of the iNP (Figure 2d). EDS mapping of a larger area with c.a. 30 particles is given as Figure S7. Both Pt and Zn are homogeneously dispersed in these particles, which further confirms the uniform compositions from particle to particle.

The electro-catalytic properties of PtZn/MWNT were studied by the methanol oxidation reaction (MOR) under both acidic and basic conditions. To enhance the conductivity, the $mSiO_2$ shell was etched from Pt/MWNT@$mSiO_2$ and PtZn/MWNT@$mSiO_2$ using 1 M

NaOH at room temperature before electrochemical tests (the last step in Figure 1a). These etched samples were labeled as Pt/MWNT-E and PtZn/MWNT-E. No obvious size increase was observed in PtZn/MWNT-E as evidenced by TEM images (Figure 1f, S4b, Table S1). ICP-MS confirmed that there's no metal loss during silica etching and the bulk Pt to Zn ratio was maintained as 1.03:1. The measured surface ratio of Pt to Zn on PtZn/MWNT-E is 1.1 by X-ray photoelectron spectroscopy (XPS) as shown in Figure S8 and Table S2. The slightly Pt-rich surface in XPS agrees with the elemental mapping in Figure 2d-f.

The typical methanol oxidation polarization curves in acidic condition for PtZn/MWNT-E, Pt/MWNT-E, and commercial Pt/Vulcan catalysts are shown in Figure 3. According to the reported mechanism,[16] methanol is first oxidized to CO_2, CO and/or other carbonaceous intermediates during the forward sweep, contributing to the current density peak at around 0.65 V relative to the Ag/AgCl reference electrode. The adsorbed carbonaceous intermediates are further oxidized to CO_2 during the backward sweep, corresponding to the current density peak at around 0.4 V. To better investigate the electrochemical behaviors of PtZn/MWNT-E, we also evaluated the control sample, PtZn/MWNT, with larger PtZn iNPs, synthesized by co-reduction of Pt and Zn precursor on naked MWNT without the $mSiO_2$ shell (the green curve in Figure 3). PtZn/MWNT-E showed the highest activity due to its lower onset potential and higher current density among all tested samples. The ratio of forward current density (J_f) to backward current density (J_b) can evaluate the tolerance of catalysts towards poisoning by carbonaceous species.[16] As shown in Figure 3a, the ratio of J_f/J_b for PtZn/MWNT-E (1.46) is much higher than PtZn/MWNT control sample (1.01), Pt/MWNT (0.83) and Pt/Vulcan (0.81) . It clearly shows that the PtZn iNP greatly enhances the tolerance of the catalyst against poisoning.

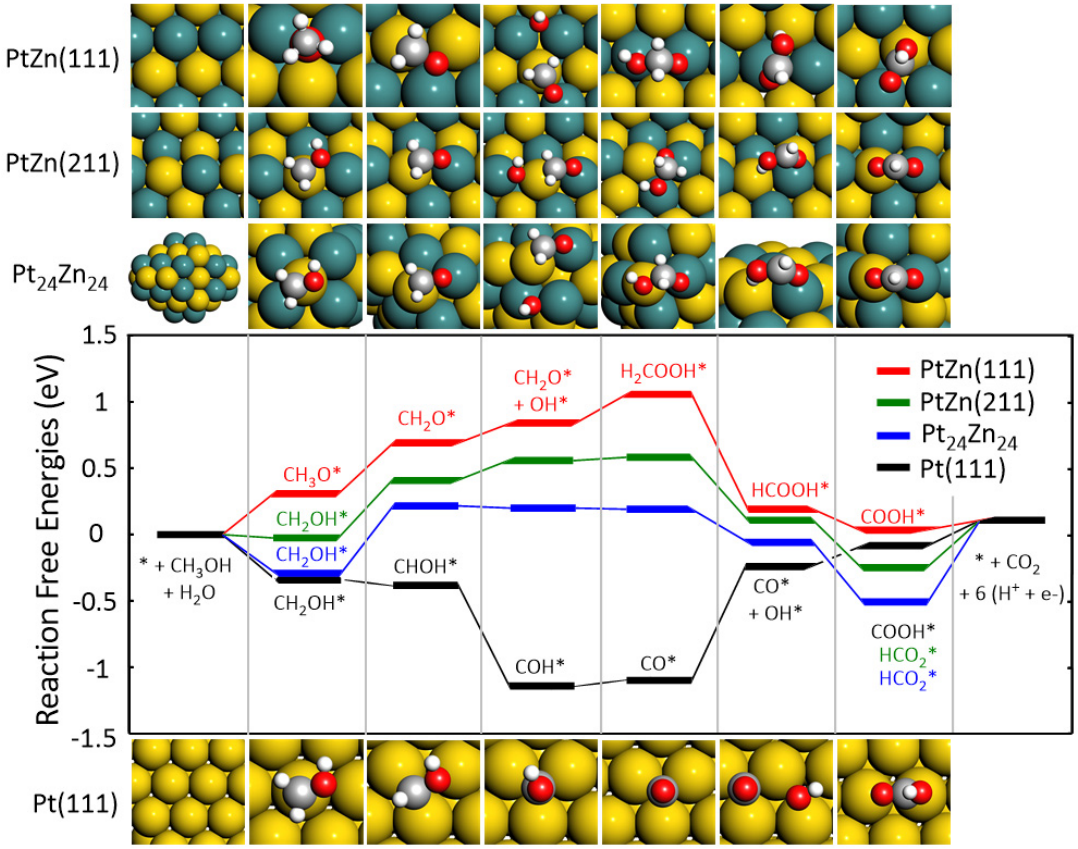

Figure 4. Calculated reaction mechanisms of MOR on PtZn (111), stepped PtZn (211), $Pt_{24}Zn_{24}$ cluster and Pt (111). For the reactions on PtZn (111), PtZn (211) and $Pt_{24}Zn_{24}$, all the elementary reaction steps, except for $CH_2O^* + OH^* \rightarrow H_2COOH^*$, involve the dissociation of a ($H^+ + e^-$) pair. For the reaction on Pt (111), all the steps, except for $CO^* + OH^* \rightarrow COOH^*$, involve the dissociation of a ($H^+ + e^-$) pair.

Figure 3b gives the chronoamperometry (CA) curves for MOR in acidic solution by holding the potential at 0.65 V vs. Ag/AgCl, which is the potential of the forward oxidation peak. The current density of PtZn/MWNT decays rapidly and becomes the smallest after 100 s. The rapid decay in activity for PtZn iNPs synthesized on MWNT without the confinement of $mSiO_2$ is because of their larger particle size. As proven previously by leaching tests performed on $PtNi_3$ nanoparticles, larger particles are more sensitive to-

wards leaching in acidic conditions, leading to lower stability over time.[31] PtZn/MWNT-E shows the highest specific and mass activities, followed by Pt/MWNT-E, Pt/Vulcan, and PtZn/MWNT, which directly shows the incorporation of Zn can enhance the MOR activity. Additionally, the smaller size of particles can also facilitate the effective utilization of Pt and further promote the activity as proven by the fact that PtZn/MWNT-E has 10 times higher mass activity than PtZn/MWNT (Figure 3c).

Activities of different catalysts towards methanol oxidation were also evaluated in a basic solution containing 0.1 M KOH and 0.5 M methanol, as shown in Figure 3d-f. PtZn/MWNT-E still shows the highest current density in both CV and CA curves. CA curves were measured by holding the potential at – 0.1 V and the current densities of different catalysts follow a similar trend as that in the CV curves over time. PtZn/MWNT is found to be not stable in basic solution as shown in Figure 3e. The specific activity of PtZn/MWNT is two times worse than PtZn/MWNT-E (Figure 3f), which indicates that the smaller size of PtZn iNPs can also enhance the MOR activity in basic condition.

To have a better insight into the structure and activity relationship, another two control samples (2.8 nm PtZn alloy/MWNT and 8.6 nm PtZn intermetallic/MWNT) were prepared (Figure S10 and S11). Their electrocatalytic performance was compared with other catalysts and summarized in Table S3 and S4. PtZn iNPs has 2.3 and 1.7 times higher specific activities in the respective acidic and basic conditions, compared to that of PtZn alloy NPs with a comparable size (Figure S12). Moreover, the specific activity increases with the decrease of the particle size. We also compared the activity of PtZn/MWNT-E with the results from previously published literature (summarized in Table S5), among which PtZn/MWNT-E has the highest mass activity, comparable specific activity, and J_f/J_b values. Therefore, the smaller PtZn iNPs is highly favorable for MOR.

Density functional theory (DFT) calculations were carried out to investigate the reaction mechanisms of MOR on PtZn and Pt materials and the effect of particle size and metal composition. The reaction free energies of each electrochemical step were calculated using the computational hydrogen electrode (CHE) model,[32-34] which is independent of the pH value of the electrolyte (for the computational details, please refer to the supporting information). Although it is challenging to calculate the MOR on nanoparticles with different sizes, it is reasonable to investigate the particle size effect by considering different reaction sites (terrace, edge, and corner), because smaller nanoparticles generally have higher ratios of edge and corner sites than larger nanoparticles.[35] Therefore, in this study PtZn (111), stepped PtZn (211) and a $Pt_{24}Zn_{24}$ cluster were calculated to represent terrace, edge, and corner sites, respectively. As shown in Figure 4, all three PtZn systems undergo a non-CO reaction pathway, in which a key intermediate CH_2O^* is formed from either CH_3O^* or CH_2OH^*, followed by its interaction with a surface hydroxyl (OH*) to form H_2COOH^*. The H_2COOH^* then releases a ($H^+ + e^-$) pair to form HCOOH*. The HCOOH* then goes through either COOH* or $HCOO^*$ to form CO_2. It is notable that the reaction pathways of the three PtZn systems follow an energetic trend: $Pt_{24}Zn_{24}$ < PtZn (211) < PtZn (111), suggesting that MOR on corner sites are likely to have smaller apparent barriers than that on edge and terrace sites. This is likely due to the enhanced binding strengths between the intermediate adsorbates and the under-coordinated metal atoms on the corner sites. This indicates that smaller PtZn iNPs are energetically more favorable for MOR than larger iNPs.

These computational results support the experimental observations that size-confined PtZn iNPs (PtZn/MWNT-E) are more active in both acidic and basic solutions than larger iNPs (PtZn/MWNT). Furthermore, the PtZn systems were compared with the Pt (111) surface to study the effect of metal composition (Figure 4). Differing from the PtZn systems, MOR on Pt (111) undergoes a CO pathway, in which CHOH* is formed after CH_2OH^*, followed by the formation of COH* and CO*. The CO* is then converted to COOH*, which is oxidized to form CO_2. This reaction pathway agrees well with a previous DFT study.[36] Although the reaction pathway of Pt (111) showed no apparent barrier, the highly stable COH* and CO* engender a "thermodynamic sink", and thus the conversion from CO* to CO_2 becomes energetically hindered (Figure 4). This could lead to the catalyst deactivation by CO poisoning. In addition, another key adsorbate, OH*, is found to have higher binding strength with Zn atoms compared to Pt atoms (Figure 4). The stabilization of OH* by Zn atoms leads to the ($CH_2O^* \rightarrow CH_2O^* + OH^* \rightarrow H_2COOH^*$) pathway for the PtZn systems instead of the ($CH_2O^* \rightarrow CHO^* \rightarrow CO^*$) pathway.

The different reaction paths between PtZn systems and pure Pt explained the experimentally observed higher tolerance of PtZn systems toward poisoning compared to commercial Pt catalyst and revealed the critical role of Zn atoms. With no remarkable barriers or thermodynamic sinks, the calculated $Pt_{24}Zn_{24}$ pathway reflects the better catalytic activity of PtZn/MWNT-E than larger PtZn iNPs and commercial Pt catalyst.

To support the non-CO pathway on PtZn surface, we conducted more experiments to study the origin of the backward oxidation peak of MOR by a previously reported method.[37] As shown in Figure S14a and c, CV scan (cycle 1) was first measured in an acidic solution without methanol. Methanol was added at the beginning of the second cathodic (backward) scan, at which point MOR intermediates have not been formed. Therefore, the backward peak observed during the second cathodic scan is purely induced by the freshly added methanol. We then compared the peak area of backward peak in the second and third cycles. The extra peak area (charge) in the third cathodic scan than the second one could be caused by intermediates generated in the third anodic (forward) scan. The fractions of contribution from intermediates were calculated as 34.8% for PtZn iNPs and 67.8% for Pt NPs,

which indicates that fewer intermediates were generated on PtZn than on Pt (Figure S14a and c). In another experiment, we purged CO at the beginning of the second cathodic scan. As shown in Figure S14d, CO was immediately oxidized on the surface of Pt as indicated by the sudden current jump, while no CO oxidization was observed on PtZn iNPs (Figure S14b). These experimental results suggest that CO has a weaker interaction with PtZn than with Pt.

Leaching of Zn was only observed after 1000 cycles in the acidic electrolyte, while basic condition does not cause any obvious leaching of Zn even after 1000 cycles (Table S6). The specific activity of PtZn/MWNT-E and Pt/Vulcan catalysts before and after 1000 cycles were compared (Figure S15). Surprisingly, only 3% loss in specific activity was observed on PtZn/MWNT-E, while commercial Pt/Vulcan has a 50 % lost. It is highly possible that the PtZn iNPs transform to particles with thin Pt shells on PtZn intermetallic cores under the acidic condition. However, the PtZn intermetallic core could still alter the electronic structure of the Pt shell and lead to the enhanced MOR performance, as proposed by Abruña group.[17]

CONCLUSION

In summary, we have successfully synthesized sub-4 nm PtZn iNPs using a general and well-controlled manner benefiting from the MWNT@mSiO_2 platform. The mSiO_2 shell provides a confined environment for the growth of metal nanoparticles and prevents them from aggregating during high-temperature annealing, a step required for the formation of PtZn intermetallic phase. The smaller PtZn iNPs synthesized by the mSiO_2 shell confinement show better stability in both acidic and basic electrolytes and higher activity than commercial Pt catalyst and the larger PtZn iNPs directly synthesized without the protection of the mSiO_2 shell. DFT calculations are in good agreement with the experimental results. The calculations reveal that PtZn systems undergo a "non-CO" pathway for MOR, due to the stabilization of OH* by Zn atoms. However, pure Pt system forms highly stable COH* and CO* intermediates, which could cause catalyst deactivation. Furthermore, the calculations demonstrate that the reaction pathways of smaller-size PtZn particles are energetically more favorable than those of larger particles, due to the enhanced adsorption energies by the under-coordinated corner atoms. This general synthesis strategy using the MWNT@mSiO_2 platform opens up fascinating opportunities for the synthesis of intermetallic nanomaterials with well-controlled particle sizes and improved monodispersity, which could lead to highly active heterogeneous catalysts with enhanced specific activity and stability in fuel cell applications.

ASSOCIATED CONTENT

SUPPORTING INFORMATION

The Supporting Information is available free of charge on the ACS Publications website. Detailed experimental procedures; additional PXRD patterns and TEM images; XPS of PtZn/MWNT-E; DFT calculation

AUTHOR INFORMATION

Corresponding Author

whuang@iastate.edu

Funding Sources

Any funds used to support the research of the manuscript should be placed here (per journal style).

Notes

The authors declare no competing financial interest.

ACKNOWLEDGMENT

This work was partially supported by National Science Foundation (NSF) grant CHE- 1607305. We are also grateful for the support by the startup funds from Ames Laboratory (Royalty Account) and Iowa State University. The work at Ames Lab was supported in part by the U.S. Department of Energy (DOE), Office of Science, Basic Energy Sciences, Materials Science and Engineering Division under Contract DE-AC02-07CH11358, with additional capabilities made possible from LDRD funding. We thank Professor Gordon J. Miller for the use of the X-ray diffractometer. The U.S. Department of Energy, Office of Science, BES-Division of Materials Science and Engineering (computational study) and BES-Scientific User Facilities under Contract DE-AC02-06CH11357 supported the computational work. We acknowledge the computing resources operated by the Laboratory Computing Resource Center (ANL) and the ANL Center for Nanoscale Materials.

REFERENCES

1. DeSario, D. Y.; DiSalvo, F. J. *Chem. Mater.* **2014,** *26* (8), 2750-2757.
2. Abe, H.; Matsumoto, F.; Alden, L. R.; Warren, S. C.; Abruna, H. D.; DiSalvo, F. J. *J. Am. Chem. Soc.* **2008,** *130* (16), 5452-5458.
3. Cui, Z. M.; Chen, H.; Zhao, M. T.; Marshall, D.; Yu, Y. C.; Abruna, H.; DiSalvo, F. J. *J. Am. Chem. Soc.* **2014,** *136* (29), 10206-10209.
4. Kang, Y. J.; Murray, C. B. *J. Am. Chem. Soc.* **2010,** *132* (22), 7568-+.
5. Ghosh, T.; Leonard, B. M.; Zhou, Q.; DiSalvo, F. J. *Chem. Mater.* **2010,** *22* (7), 2190-2202.
6. Yang, H. Z.; Zhang, J.; Sun, K.; Zou, S. Z.; Fang, J. Y. *Angew Chem Int Edit* **2010,** *49* (38), 6848-6851.
7. Liu, L. F.; Pippel, E.; Scholz, R.; Gosele, U. *Nano Lett.* **2009,** *9* (12), 4352-4358.
8. Wang, D. L.; Xin, H. L. L.; Hovden, R.; Wang, H. S.; Yu, Y. C.; Muller, D. A.; DiSalvo, F. J.; Abruna, H. D. *Nat. Mater.* **2013,** *12* (1), 81-87.
9. Chen, W.; Kim, J. M.; Sun, S. H.; Chen, S. W. *Langmuir* **2007,** *23* (22), 11303-11310.
10. Wang, D. Y.; Chou, H. L.; Lin, Y. C.; Lai, F. J.; Chen, C. H.; Lee, J. F.; Hwang, B. J.; Chen, C. C. *J. Am. Chem. Soc.* **2012,** *134* (24), 10011-10020.

11. Casado-Rivera, E.; Volpe, D. J.; Alden, L.; Lind, C.; Downie, C.; Vazquez-Alvarez, T.; Angelo, A. C. D.; DiSalvo, F. J.; Abruna, H. D. *J. Am. Chem. Soc.* **2004,** *126* (12), 4043-4049.
12. Ji, X. L.; Lee, K. T.; Holden, R.; Zhang, L.; Zhang, J. J.; Botton, G. A.; Couillard, M.; Nazar, L. F. *Nat. Chem.* **2010,** *2* (4), 286-293.
13. Matsumoto, F.; Roychowdhury, C.; DiSalvo, F. J.; Abruna, H. D. *J. Electrochem. Soc.* **2008,** *155* (2), B148-B154.
14. Stamenkovic, V. R.; Fowler, B.; Mun, B. S.; Wang, G. F.; Ross, P. N.; Lucas, C. A.; Markovic, N. M. *Science* **2007,** *315* (5811), 493-497.
15. Miura, A.; Wang, H. S.; Leonard, B. M.; Abruna, H. D.; DiSalvo, F. J. *Chem. Mater.* **2009,** *21* (13), 2661-2667.
16. Kang, Y. J.; Pyo, J. B.; Ye, X. C.; Gordon, T. R.; Murray, C. B. *ACS Nano* **2012,** *6* (6), 5642-5647.
17. Gregoire, J. M.; Kostylev, M.; Tague, M. E.; Mutolo, P. F.; van Dover, R. B.; DiSalvo, F. J.; Abruna, H. D. *J. Electrochem. Soc.* **2009,** *156* (1), B160-B166.
18. Chen, Q. L.; Zhang, J. W.; Jia, Y. Y.; Jiang, Z. Y.; Xie, Z. X.; Zheng, L. S. *Nanoscale* **2014,** *6* (12), 7019-7024.
19. Xu, D.; Liu, Z. P.; Yang, H. Z.; Liu, Q. S.; Zhang, J.; Fang, J. Y.; Zou, S. Z.; Sun, K. *Angew. Chem. Int. Edit.* **2009,** *48* (23), 4217-4221.
20. Xia, B. Y.; Wu, H. B.; Wang, X.; Lou, X. W. *J. Am. Chem. Soc.* **2012,** *134* (34), 13934-13937.
21. Sun, X. H.; Jiang, K. Z.; Zhang, N.; Guo, S. J.; Huang, X. Q. *ACS Nano* **2015,** *9* (7), 7634-7640.
22. Saleem, F.; Zhang, Z. C.; Xu, B.; Xu, X. B.; He, P. L.; Wang, X. *J. Am. Chem. Soc.* **2013,** *135* (49), 18304-18307.
23. An, K.; Alayoglu, S.; Musselwhite, N.; Plamthottam, S.; Melaet, G.; Lindeman, A. E.; Somorjai, G. A. *J. Am. Chem. Soc.* **2013,** *135* (44), 16689-16696.
24. An, K.; Alayoglu, S.; Musselwhite, N.; Na, K.; Somorjai, G. A. *J. Am. Chem. Soc.* **2014,** *136* (19), 6830-6833.
25. Li, W.; Yang, J. P.; Wu, Z. X.; Wang, J. X.; Li, B.; Feng, S. S.; Deng, Y. H.; Zhang, F.; Zhao, D. Y. *J. Am. Chem. Soc.* **2012,** *134* (29), 11864-11867.
26. Shang, L.; Bian, T.; Zhang, B.; Zhang, D.; Wu, L.-Z.; Tung, C.-H.; Yin, Y.; Zhang, T. *Angew. Chem. Int. Edit.* **2014,** *53* (1), 250-254.
27. Xiao, C.; Maligal-Ganesh, R. V.; Li, T.; Qi, Z.; Guo, Z.; Brashler, K. T.; Goes, S.; Li, X.; Goh, T. W.; Winans, R. E.; Huang, W. *ChemSusChem* **2013,** *6* (10), 1915-1922.
28. Maligal-Ganesh, R.; Xiao, C.; Goh, T.; Wang, L.; Gustafson, J.; Pei, Y.; Qi, Z.; Jahson, D. D.; Zhang, S.; Tao, F.; Huang, W. *ACS Catal.* **2016,** *6* (3), 1754-1764.
29. Pei, Y.; Maligal-Ganesh, R.; Xiao, C.; Goh, T.; Brashler, K.; Gustafson, J.; Huang, W. *Nanoscale* **2015,** *7*, 16721-16728.
30. Fang, B.; Chaudhari, N. K.; Kim, M. S.; Kim, J. H.; Yu, J. S. *J. Am. Chem. Soc.* **2009,** *131* (42), 15330-15338.
31. Gan, L.; Heggen, M.; O'Malley, R.; Theobald, B.; Strasser, P. *Nano Lett.* **2013,** *13* (3), 1131-1138.
32. Peterson, A. A.; Abild-Pedersen, F.; Studt, F.; Rossmeisl, J.; Norskov, J. K. *Energ. Environ. Sci.* **2010,** *3* (9), 1311-1315.
33. Norskov, J. K.; Rossmeisl, J.; Logadottir, A.; Lindqvist, L.; Kitchin, J. R.; Bligaard, T.; Jonsson, H. *J. Phys. Chem. B* **2004,** *108* (46), 17886-17892.
34. Peterson, A. A.; Norskov, J. K. *J. Phys. Chem. Lett.* **2012,** *3* (2), 251-258.
35. Gao, D. F.; Zhou, H.; Wang, J.; Miao, S.; Yang, F.; Wang, G. X.; Wang, J. G.; Bao, X. H. *J. Am. Chem. Soc.* **2015,** *137* (13), 4288-4291.
36. Ferrin, P.; Mavrikakis, M. *J. Am. Chem. Soc.* **2009,** *131* (40), 14381-14389.
37. Zhao, Y. Z.; Li, X. M.; Schechter, J. M.; Yang, Y. A. *RSC Adv.* **2016,** *6* (7), 5384-5390.

Table of Content